Neuron, Volume *68*

Supplemental Information

Genetic Mosaic Dissection of *Lis1* and *Ndel1* in Neuronal Migration

Simon Hippenmeyer, Yong Ha Youn, Hyang Mi Moon, Kazunari Miyamichi, Hui Zong, Anthony Wynshaw-Boris, and Liqun Luo

INVENTORY:

Supplemental Figures with Legends

Supplemental Movies

Supplemental Experimental Procedures

Supplemental References

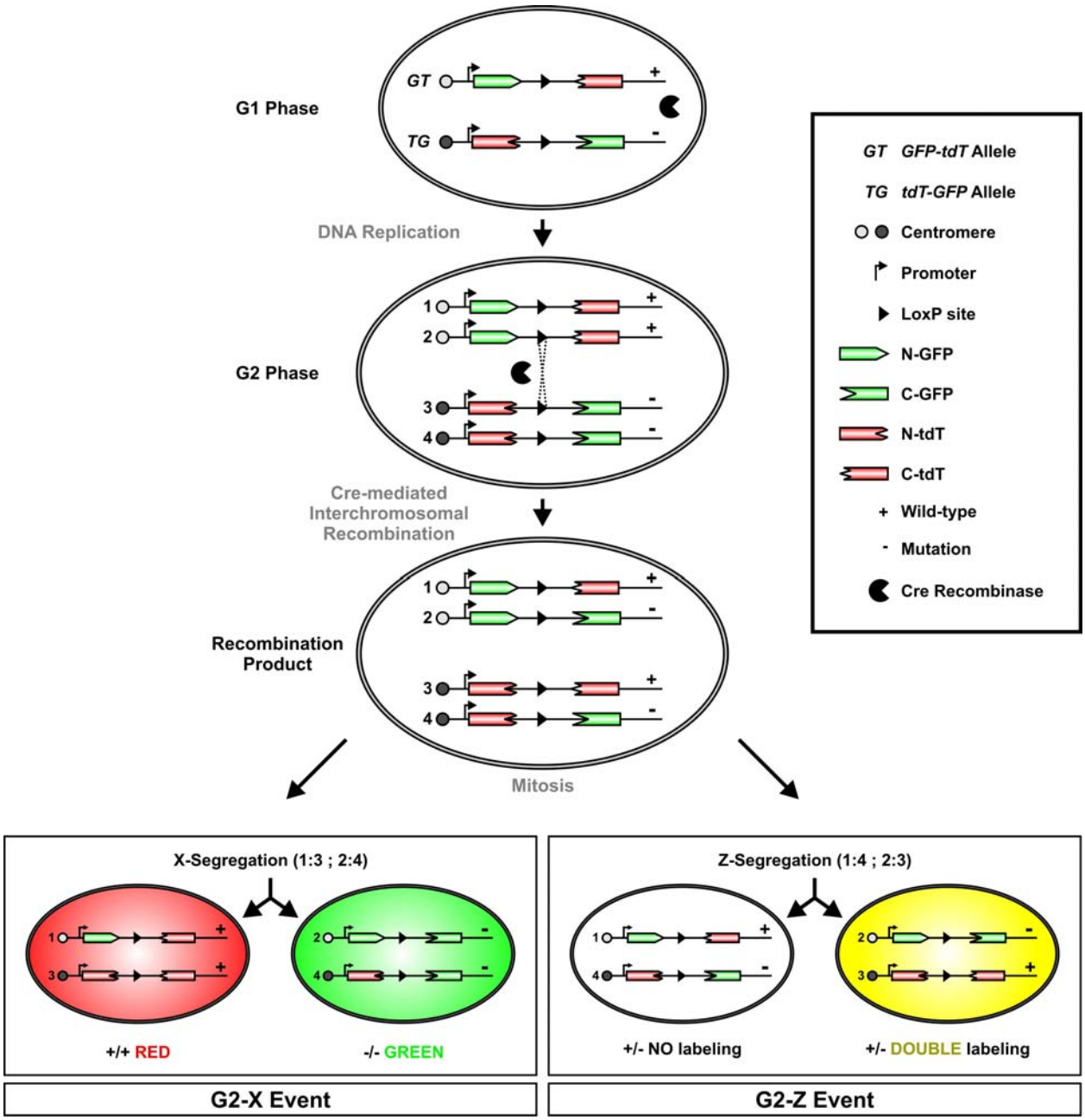

Figure S1. Principle of MADM, Related to Figure 1.

MADM employs Cre/LoxP-dependent interchromosomal recombination to generate uniquely labeled homozygous mutant cells in an otherwise heterozygous background in mice. Two reciprocally chimeric marker genes are targeted separately to identical loci on homologous chromosomes (here *Hipp11* for MADM-11). The chimeric marker genes (labeled as *GT* and *TG* alleles) consist of partial coding sequences for green (eGFP[G]) and red (tdT[T], tandem dimer Tomato) fluorescent proteins separated by an intron containing the LoxP site. MADM-11 contains an additional FRT site that allows the induction of MADM-labeling by the FLP recombinase. Following recombinase-mediated interchromosomal recombination, functional

green and red fluorescent proteins are reconstituted. If recombination occurred at the G2 phase and the two recombinant chromosomes were segregated into different daughter cells (X-Segregation, left branch; we term these G2-X events), each daughter cell would express a single fluorescent protein. When a mutation of interest is introduced distal to one MADM cassette, then one of the daughter cells would be homozygous mutant (here the green cell) for the gene of interest, whereas its sibling, labeled by a different color (red), would be homozygous wild-type. In addition to G2-X events, recombination in G2 followed by Z-Segregation (G2-Z events, right branch), G1, or postmitotic recombinations (not shown) do not alter the heterozygote genotype, but can produce double-labeled (yellow) cells. Note that the direction of transcription of the transgenes from *MADM-11* (proximal to distal with the centromere as reference) is opposite to the direction of transcription from the original MADM at the *Rosa26* locus (distal to proximal; Zong et al., 2005).

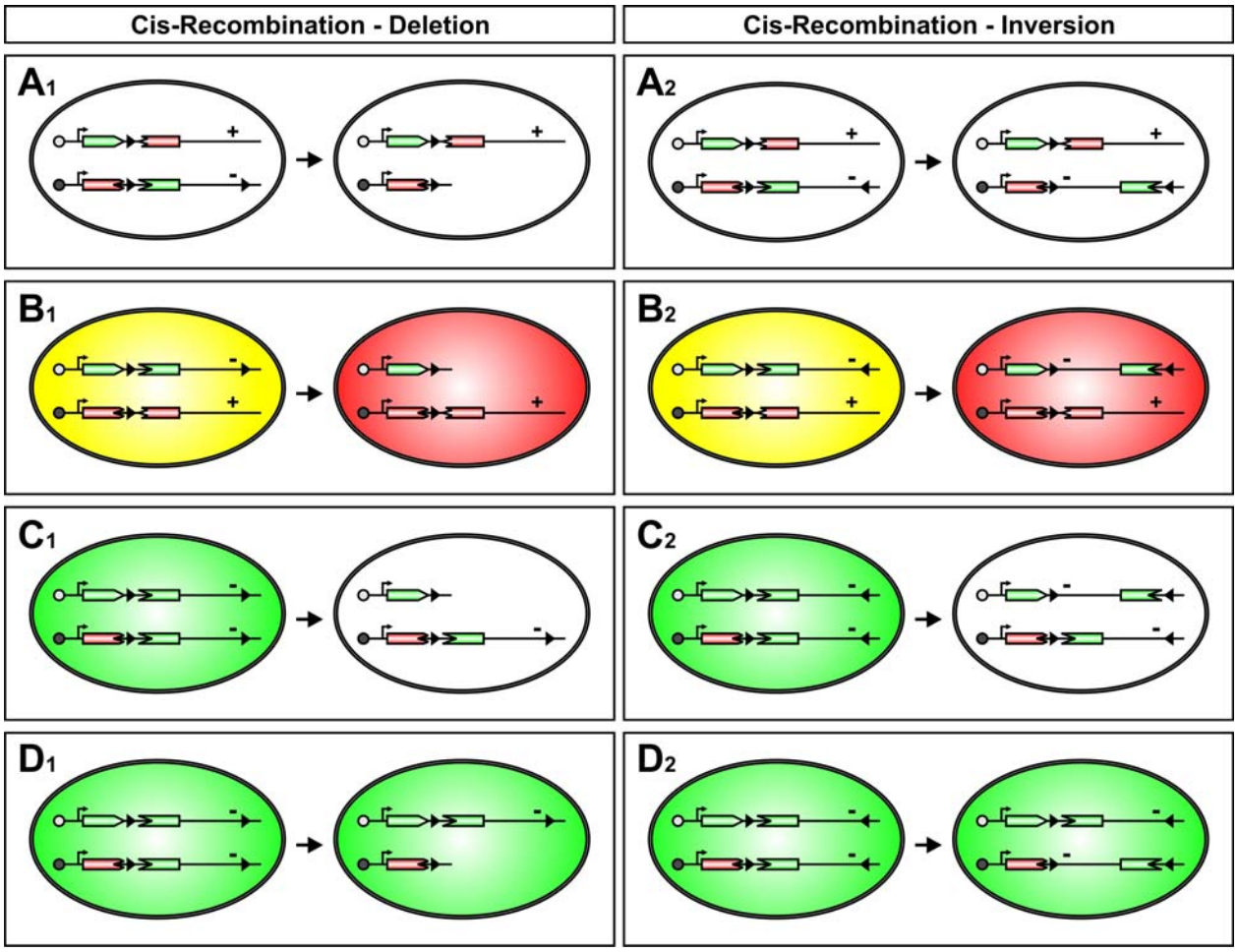

Figure S2. Possible Effect of LoxP Sites at Targeted Knockout Loci for MADM Analysis, Related to Figures 1 and 2.

MADM-11 provides a genetic mosaic analysis resource for mutations located on Chr. 11 distal to *Hipp11*. However, given that a significant number of targeted mutations contain LoxP sites (such as the three mutations in *Lis1*, *Ndel1* and *14-3-3ε* analyzed in this study), there is a possibility that intra-chromosomal cis-recombination with the LoxP site in the MADM cassettes could occur in the absence of, or in combination with, MADM-mediated inter-chromosomal recombination. Such cis-recombination events would cause inversion or deletion depending on the orientation of the LoxP site in target loci. Previous studies in ES cells have provided an estimate for such cis-recombination events (Zheng et al., 2000). If cis-recombination resulted in inversions and therefore unlikely to cause lethality in ES cells (as oppose to deletions which likely cause ES cells to die), the rate of inversion was estimated to be $2.2x10^{-3}$, $3.2x10^{-4}$, and $8.3x10^{-5}$ for distances of 24, 30 and 60 cM (Zheng et al., 2000). Given the large distance between MADM cassette near the centromere and the three target loci we analyzed (>40 cM), we expect a low rate of cis-recombination. Nevertheless, we have modeled the consequence if such events do happen [for simplicity, we assume that the mutant allele is linked with the green GFP marker (TG), as in most of our experiments; see Figure S1 for complete MADM scheme]:

(A) If the trans-recombination between the MADM cassettes does not occur, cis-recombinations alone that cause deletion (A_1) or inversion (A_2) would not produce labeled cells and therefore should not affect the outcome of MADM analysis, which focuses on labeled cells.
(B) In +/- yellow cells that were generated by G2-Z, G1 and postmitotic recombinations, cis-recombination can only occur on the green chromosome that carries the mutation. This would result in loss of the green marker and the cell would turn from yellow to red. In addition this red cell will carry an additional deletion (B_1) or inversion (B_2), depending on the loxP orientation.
(C-D) In -/- green cells, there are two possibilities. If cis-recombination occurs on the recombinant chromosome (C), the green marker would be disrupted, resulting in the loss of color. The frequency of green cells in MADM labeling is consequently reduced. If cis-recombination occurs on the non-recombinant chromosome (D), the resulting cell would still be green, but will carry an additional deletion (D_1) or inversion (D_2).
Additionally, in +/+ cells (not shown), no cis-recombination occurs because there is no mutant allele carrying the additional loxP site.

According to the LoxP orientations in the three alleles we analyzed, cis-recombination in *Lis1* and *Ndel1* should result in large deletions, whereas cis-recombination in *14-3-3ε* should result in an inversion. We can apply the above scenario to our mutants to estimate cis-recombination frequency.

Assuming that inversions cause little effect on the viability of cells (Zheng et al., 1999), these events should reduce the number of green cells (C_2) and increase the number of red cells (B_2) and therefore reduce green/red ratio. Yet in our *14-3-3ε* mutant neuron and glia counts, we found green/red ratio to be indistinguishable from 1:1 (Figure 2F, S5D and S6, data not shown). These results suggest that the frequency of such cis-recombination is negligible.

For deletion events, if they result in cell lethality due to partial monosomy of Chr. 11, then green cells would be reduced (C_1, D_1) but red cells would not increase (red cells die in B_1). If such deletions are compatible with cell viability, then the situation is similar to inversion discussed above. In both cases we expect to see a reduction of the green/red ratio if the frequency of such cis-recombination is significant. For *Ndel1*, cis-recombination events would delete most of Chr. 11, and would cause reduction of green/red ratio if such events happen frequently. However, Figure 2F and 6Q shows that the green/red ratio is not different from 1 in *Ndel1*-MADM.

Taken together, these conclusions are consistent with previous data in ES cells (Zheng et al., 2000) that the frequency of Cre-LoxP mediated cis-recombination occurs rarely if the genomic distance between the LoxP sequences is sufficiently large, and therefore should not affect the outcome of phenotypic analysis using MADM.

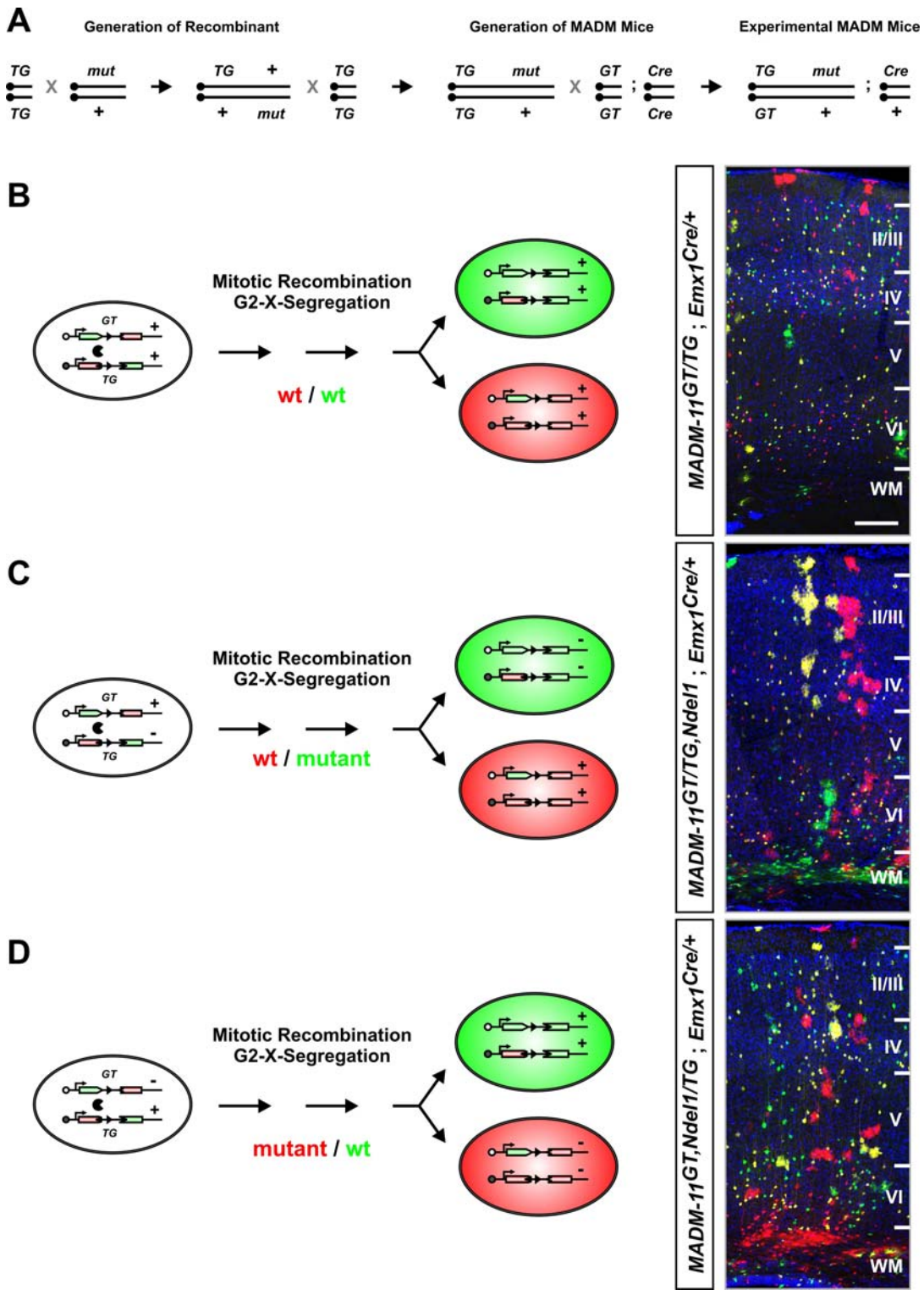

Figure S3. General Breeding Scheme and Results for Reciprocal *Ndel1*-MADM Analysis, Related to Figure 2.

(A) Breeding strategy to generate recombinant (2 crosses) and experimental (1 cross) MADM-mice. Using this strategy, the mutant cells will be labeled in green as seen throughout most of the

study, including the cells in panel S3C, as well as in the schematic depicted in Figure S1. First cross: homozygous *MADM-11*$^{TG/TG}$ is crossed to heterozygous *mutant*$^{+/-}$. Second cross: double heterozygote *MADM-11*$^{TG,+/+,mutant}$ is backcrossed to homozygous *MADM-11*$^{TG/TG}$ and meiotic recombinants between the *mutant* allele and the *TG* allele are selected. Third cross: *MADM-11*$^{TG,mutant/TG,+}$ is crossed to *MADM-11*$^{GT/GT}$;*X*$^{Cre/Cre}$ (where X represents any locus with Cre recombinase inserted as transgene). Typically, *MADM-11*$^{GT/TG,mutant}$;*X*$^{Cre/+}$ were selected with mutant cells labeled in green and wt cells labeled in red (mutant-MADM), and *MADM-11*$^{GT/TG}$;*X*$^{Cre/+}$ were used as control (control-MADM). Homozygous mutant cells can also be labeled in red and their homozygous wild-type siblings in green by reversing the crossing scheme with respect to *GT* and *TG* alleles to create a *GT, mutant* recombinant in the first cross (see Figure S3D as an example).

(B-D) Examples of MADM-labeled cells in mosaics in the somatosensory cortex using *Emx1*$^{Cre/+}$ with control-MADM (B) (*MADM-11*$^{GT/TG}$;*Emx1*$^{Cre/+}$) and mutant-MADM where mutant cells are green (C) (*MADM-11*$^{GT/TG,Ndel1}$;*Emx1*$^{Cre/+}$) or red (D) (*MADM-11*$^{GT,Ndel1/TG}$;*Emx1*$^{Cre/+}$). It is evident that *Ndel1*$^{-/-}$ neurons (but not astrocytes), whether labeled in green (C) or red (D), exhibit severe migration defects. Cortical layers are indicated in roman digits, WM: white matter. Scale bar, 150μm.

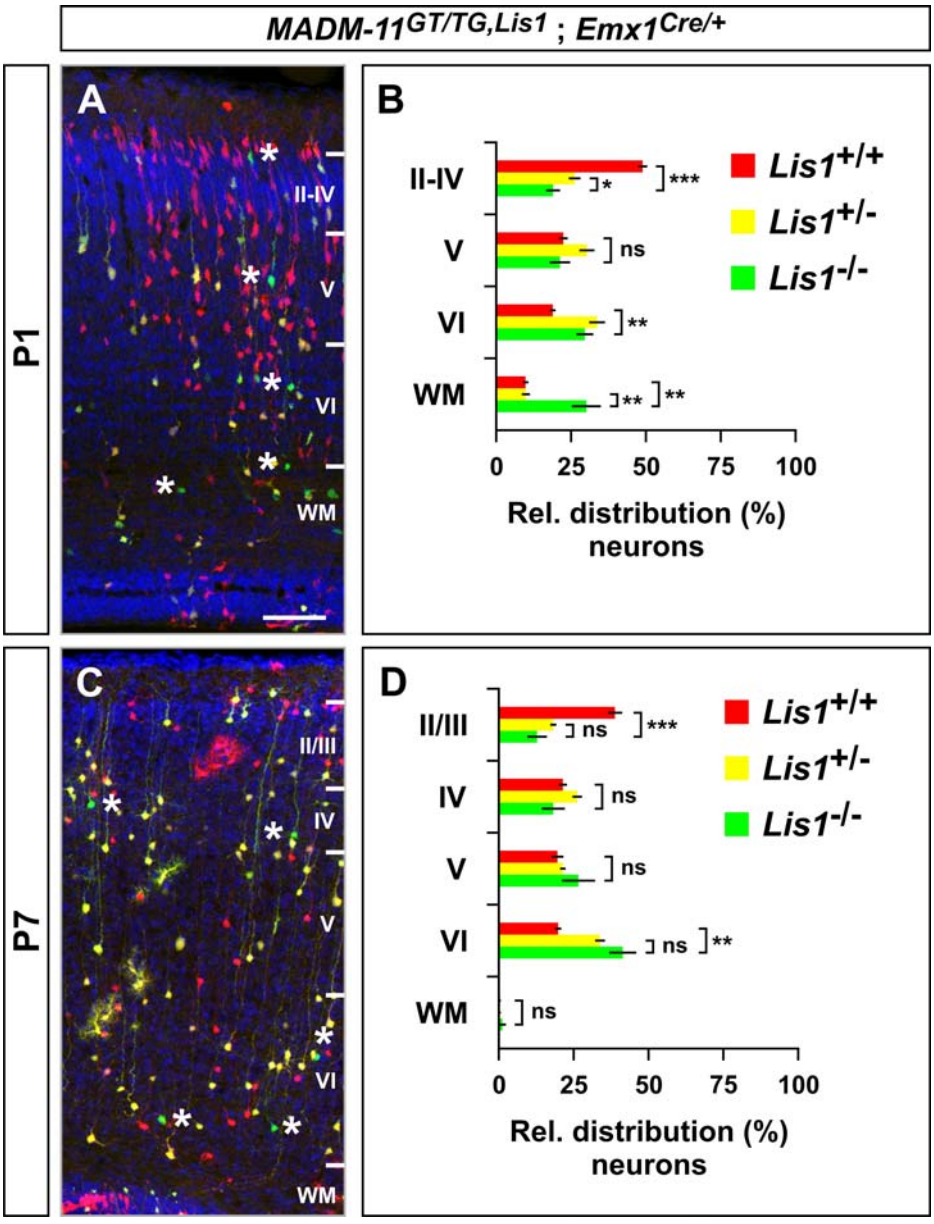

Figure S4. MADM Analysis of *Lis1* in Cortical Development, Related to Figure 2.

Time course analysis of the migration pattern of cortical projection neurons in *Lis1*-MADM (*MADM-11*$^{GT/TG,Lis1}$;*Emx1*$^{Cre/+}$) at P1 (A and B) and P7 (C and D). Mutant *Lis1*$^{-/-}$ cells are labeled with GFP (green only), heterozygous *Lis1*$^{+/-}$ cells are GFP/tdT double positive (yellow) or unlabeled (vast majority), and *Lis1*$^{+/+}$ cells are marked with tdT (red only). Nuclei were stained using DAPI (blue). White stars (A and C) indicate sparse green *Lis1*$^{-/-}$ mutant neurons. Cortical layers are numbered in roman digits. WM: white matter. Quantification charts (B and D) indicate the relative distribution (%) of mutant green, heterozygote yellow and wt red neurons. Values represent mean ± SEM. ns: non-significant, *p<0.05, **p<0.01, and ***p<0.001. Scale bar, 50μm (A); 90μm (C).

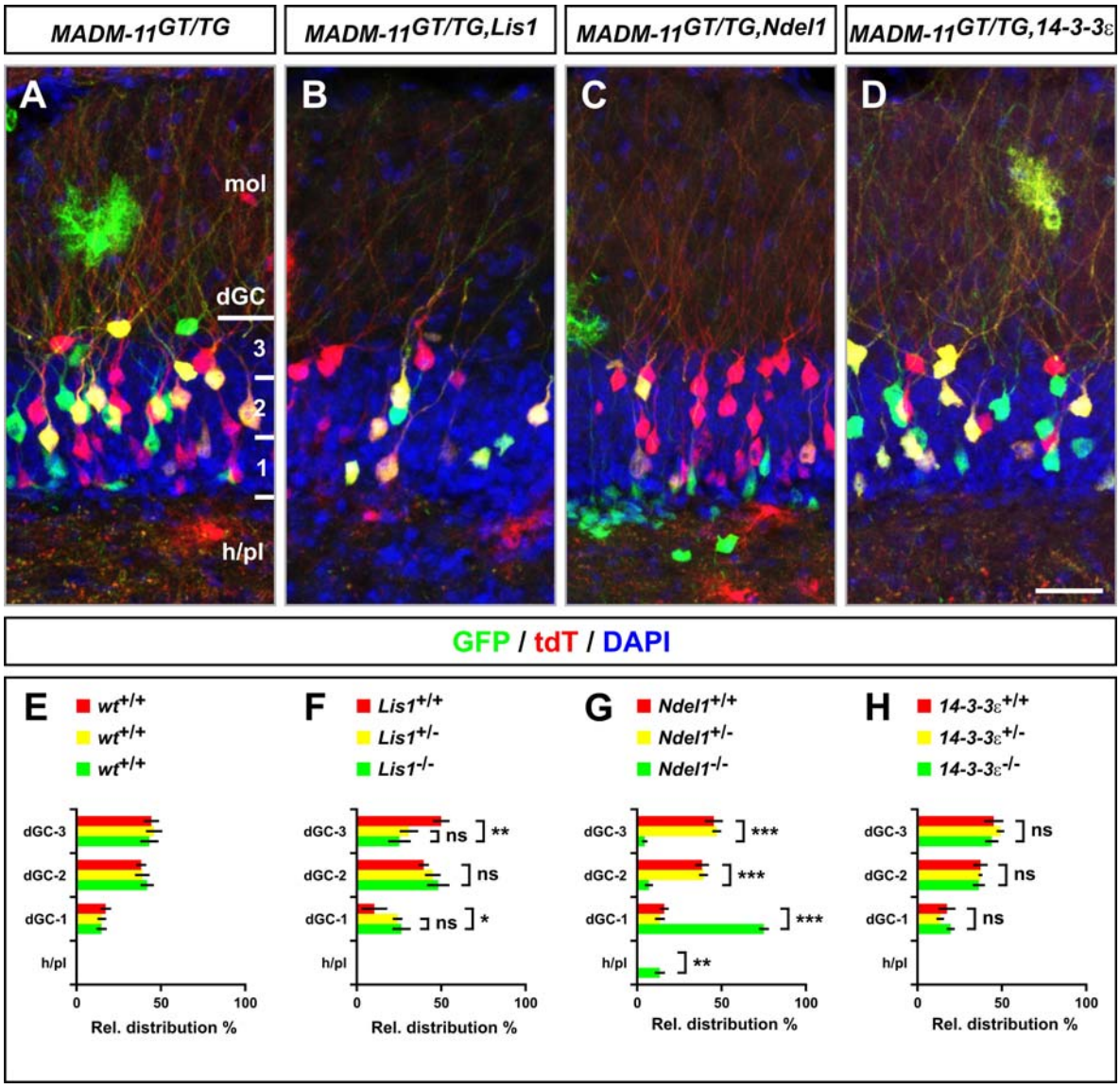

Figure S5. MADM Analysis of *Lis1*, *Ndel1* and *14-3-3ε* in Hippocampal Dentate Gyrus Granule Cell Layer, Related to Figure 3.

Distribution of MADM-labeled dGCs in the hippocampus of control-MADM (A and E; *MADM-11*$^{GT/TG}$;*Emx1*$^{Cre/+}$), *Lis1*-MADM (B and F; *MADM-11*$^{GT/TG,Lis1}$;*Emx1*$^{Cre/+}$), *Ndel1*-MADM (C and G; *MADM-11*$^{GT/TG,Ndel1}$;*Emx1*$^{Cre/+}$) and *14-3-3ε*-MADM (D and H; *MADM-11*$^{GT/TG,14\text{-}3\text{-}3\varepsilon}$;*Emx1*$^{Cre/+}$). Nuclei were stained using DAPI (blue). Scale bar, 40μm.

For quantification (E-H) of the relative distribution (%) of dGCs, the dentate gyrus was divided into three equal horizontal sectors as seen in (A). Note the significant fraction of green *Ndel1*$^{-/-}$ dGCs in the hilus/polymorphic layer below sector 1 (h/pl). Occasionally green *Ndel1*$^{-/-}$ and *Lis1*$^{-/-}$ dGCs were found in the stratum moleculare (mol). Values represent mean ± SEM. ns: non-significant, *p<0.05, **p<0.01, and ***p<0.001.

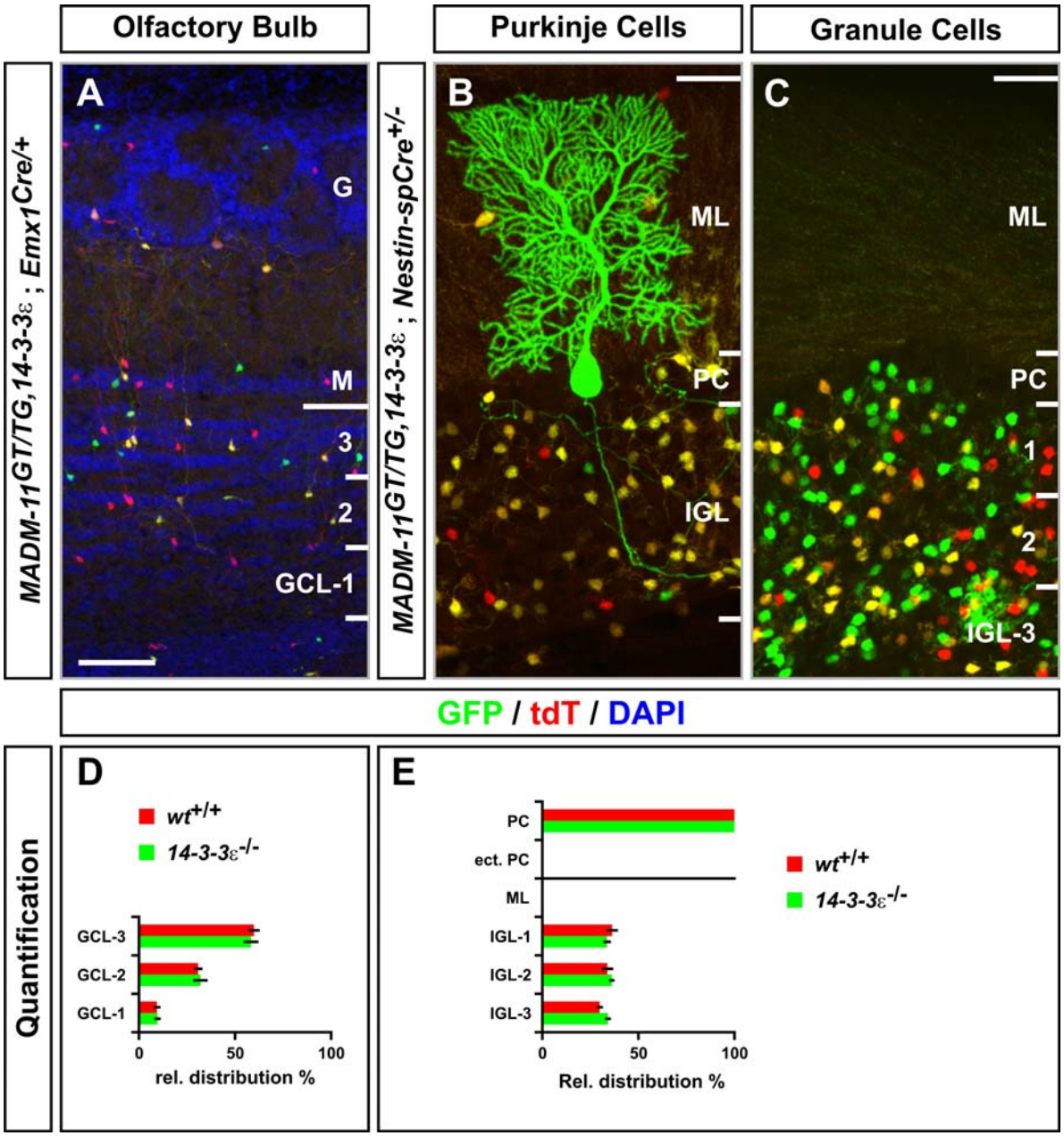

Figure S6. MADM Analysis of *14-3-3ε* in Olfactory Bulb and Cerebellum, Related to Figure 4 and Figure 5.

(A-C) Distribution of olfactory bulb interneurons (oINs) in the olfactory bulb (A), and Purkinje cells (B) and cGCs (C) in the cerebellum in P21 *MADM-11*$^{GT/TG,14\text{-}3\text{-}3\varepsilon}$;*Emx1*$^{Cre/+}$ (A) and *MADM-11*$^{GT/TG,14\text{-}3\text{-}3\varepsilon}$;*Nestin-spCre*$^{+/-}$ (B and C). Mutant *14-3-3ε*$^{-/-}$ cells are labeled with GFP (green only), heterozygous *14-3-3ε*$^{+/-}$ cells are GFP/tdT double positive (yellow) or unlabeled, and *14-3-3ε*$^{+/+}$ cells are marked with tdT (red). Nuclei in (A) were stained using DAPI (blue). Scale bar, 90μm in (A); 40μm in (B and C).

(D) Quantification of relative distribution (%) of oINs across three equal sectors in the granule cell layer (GCL) in the olfactory bulb in *14-3-3ε*-MADM. G: glomerular layer; M: mitral cell layer.

(E) Quantification of relative distribution (%) of Purkinje cells in Purkinje cell (PC) layer or ectopic locations (ect. PC); and cGCs across the molecular (ML) and internal granule cell layer (IGL) in *14-3-3ε*-MADM. The IGL was divided into three equal sectors for quantification of the relative distribution of cGCs. Values represent mean ± SEM. Note that no difference was observed in the distribution of mutant $14\text{-}3\text{-}3\varepsilon^{-/-}$ oINs, Purkinje cells and cGCs when compared to control $14\text{-}3\text{-}3\varepsilon^{+/+}$ cells.

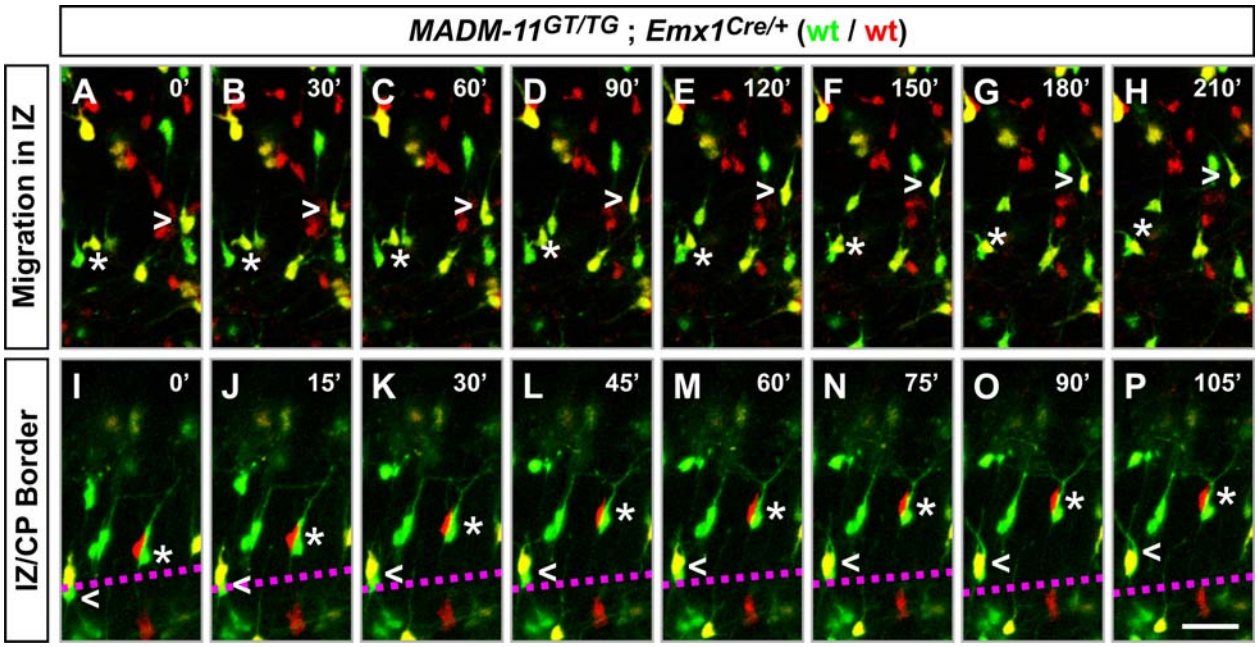

Figure S7. Live-Imaging of MADM-labeled Wild-type Cortical Projection Neurons, Related to Figure 7.

Time-lapse images of migrating cortical projection neurons in the IZ (A-H) and at the border to the CP (I-P) in cortical slices derived from control-MADM (*MADM-11*$^{GT/TG}$;*Emx1*$^{Cre/+}$) mice at E14.5. Open arrowheads and stars mark migrating green (GFP), red (tdT) and yellow (GFP^{+}/tdT^{+}) wild-type neurons. The border between the IZ and CP is indicated as dotted line in magenta (I-P). Frames are at 30' (A-H) and 15' (I-P). Scale bar, 50μm in (A-H); 40μm in (I-P).

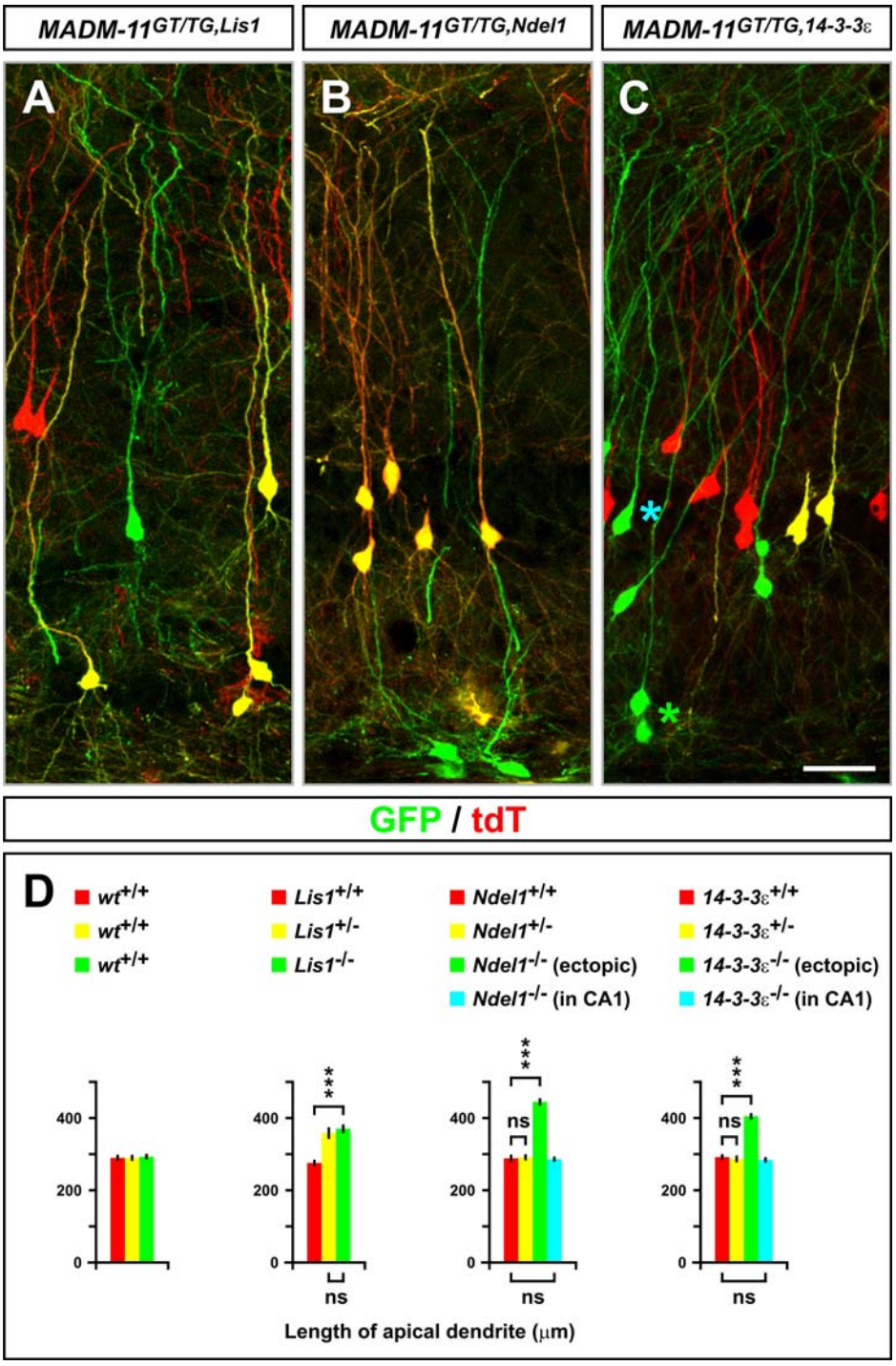

Figure S8. Analysis of Apical Dendrite Morphology in CA1 Pyramidal Cells, Related to Figure 8.

(A-C) Dendrite pattern in pyramidal CA1 cells in the hippocampus in P21 *Lis1*-MADM (A; *MADM-11*$^{GT/TG,Lis1}$;*Emx1*$^{Cre/+}$), *Ndel1*-MADM (B; *MADM-11*$^{GT/TG,Ndel1}$;*Emx1*$^{Cre/+}$), and *14-3-3ε*-MADM (C; *MADM-11*$^{GT/TG,14\text{-}3\text{-}3\varepsilon}$;*Emx1*$^{Cre/+}$). Mutant *Lis1*$^{-/-}$ (A), *Ndel1*$^{-/-}$ (B) and *14-3-3ε*$^{-/-}$ (C)

cells are labeled with GFP (green); heterozygous *Lis1*$^{+/-}$ (A), *Ndel1*$^{+/-}$ (B) and *14-3-3ε*$^{+/-}$ (C) are GFP/tdT double positive (yellow) or unlabeled; and homozygous wt *Lis1*$^{+/+}$ (A), *Ndel1*$^{+/+}$ (B) and *14-3-3ε*$^{+/+}$ (C) cells are marked with tdT (red). Cyan star in (C) marks mutant *14-3-3ε*$^{-/-}$ located in CA1 and green star in (C) marks ectopically located *14-3-3ε*$^{-/-}$ cells. In rare cases, mutant *Ndel1*$^{-/-}$ were observed in CA1 (see quantification below) but the vast majority of mutant *Ndel1*$^{-/-}$ pyramidal cells were located at the base of the CA1 field. See also Figure 3 for quantification of relative distribution and distance of cell body from base of hippocampus in control-MADM, *Lis1*-MADM, *Ndel1*-MADM and *14-3-3ε*-MADM. Scale bar, 40μm.

(D) Quantification of the length (μm) of apical CA1 pyramidal cell dendrites in the hippocampus in control-MADM, *Lis1*-MADM, *Ndel1*-MADM and *14-3-3ε*-MADM. Note the increased length of ectopically located *Lis1*$^{-/-}$, *Lis1*$^{+/-}$, *Ndel1*$^{-/-}$ (but not *Ndel1*$^{+/-}$ or rare *Ndel1*$^{-/-}$ located in CA1), and *14-3-3ε*$^{-/-}$ (but not *14-3-3ε*$^{+/-}$ or *14-3-3ε*$^{-/-}$ located in CA1). Values represent mean ± SEM. ns: non-significant, ***$p<0.001$.

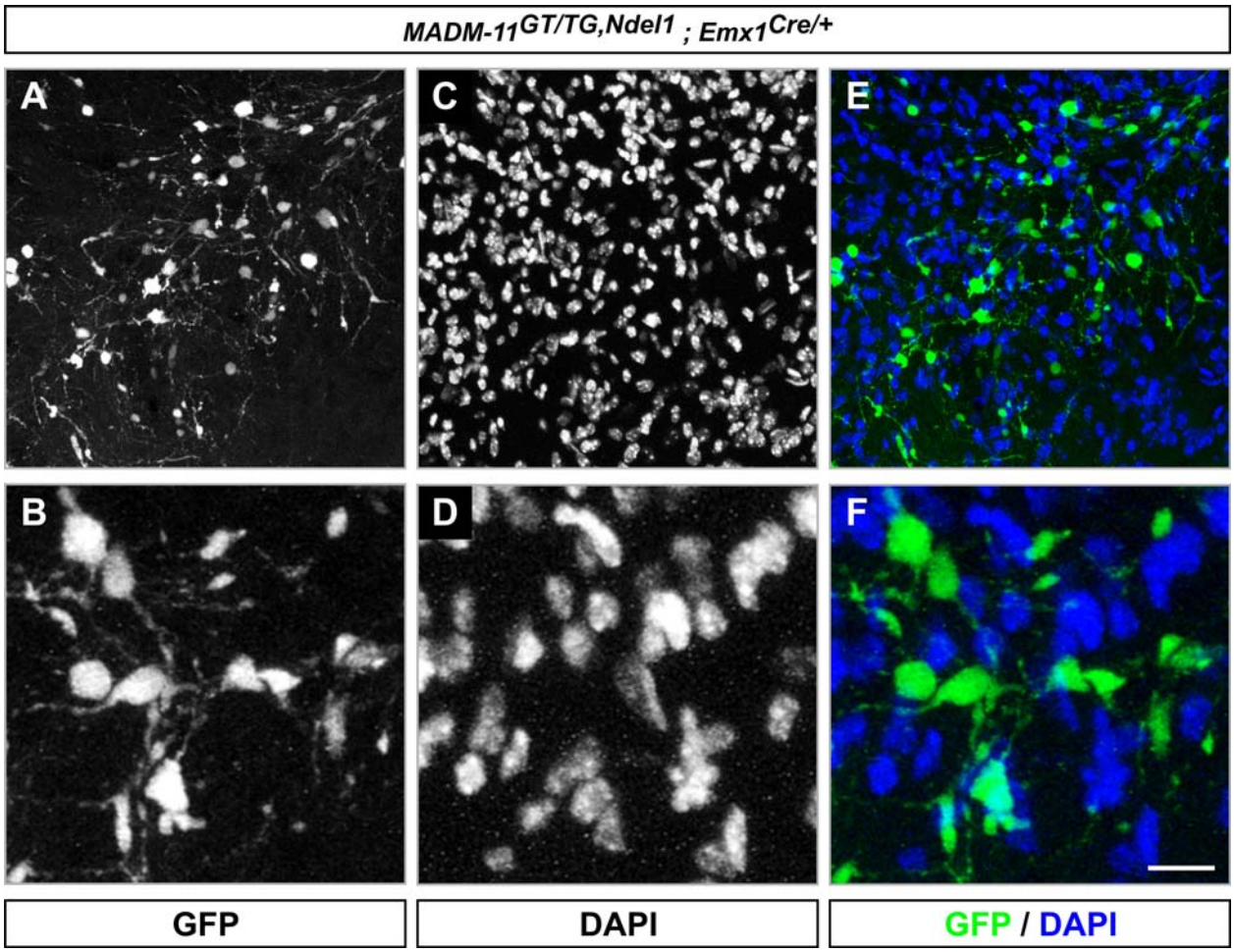

Figure S9. Variability in the Morphology of Axonal Varicosities in *Ndel1*$^{-/-}$ Cortical Projection Neurons, Related to Figure 8.

Pattern of axonal varicosities within the internal capsule in P21 *Ndel1*-MADM (*MADM-11*$^{GT/TG,Ndel1}$;*Emx1*$^{Cre/+}$) in overview (A, C and E) and at high resolution (B, D and F). Mutant *Ndel1*$^{-/-}$ subcortical projecting axons are labeled with GFP (white in A and B; green in E and F) and DAPI (white in C and D; blue in E and F) marks nuclei. Note that axonal varicosities are highly variable in size and shape and do not co-localize with DAPI. Scale bar, 40μm in (A, C and E); 10μm in (B, D and F).

SUPPLEMENTAL MOVIES

Movie S1. Related to Figure 7. Live-imaging of MADM-labeled green, red, and yellow wild-type migrating cortical projection neurons at the IZ-CP border in control-MADM at E14.5 over the course of 7h30min.

Movie S2. Related to Figure 7. Live-imaging of MADM-labeled green *Ndel1*$^{-/-}$, yellow *Ndel1*$^{+/-}$ and red *Ndel1*$^{+/+}$ migrating cortical projection neurons at the IZ-CP border in *Ndel1*-MADM at E14.5 over the course of 11h15min.

SUPPLEMENTAL EXPERIMENTAL PROCEDURES

Construction of MADM-11 Transgenes by Targeted Knockin and Mouse Genetic Techniques

Modified chimeric GT and TG MADM-cassettes were generated by splitting coding sequences for eGFP (Zong et al., 2005), and tdT (Shaner et al., 2004) tagged at the C-terminus with 3xMyc epitope, with an intron that contains a LoxP-neo-LoxP cassette (Zong et al., 2005) as well as an additional FRT site. *GT* and *TG* marker genes: *GT*: $GFP_{N\text{-}term\ (1\text{-}273)}$ - intron - $tdT_{C\text{-}term\ (4\text{-}1544)}$ and *TG*: $tdT_{N\text{-}term\ (1\text{-}3)}$ - intron - $GFP_{C\text{-}term\ (274\text{-}724)}$.

The genomic *Hipp11* locus for targeting the MADM cassettes was cloned by PCR amplification from 129/SvJ genomic DNA. GT and TG MADM-cassettes were inserted at *Hipp11* to construct GT and TG targeting vectors, which were linearized and electroporated into R1 ES cells. Two correctly targeted ES clones for each GT and TG were injected into blastocyst embryos to generate chimeric mice. All MADM experiments were carried out in mixed 129/C57Bl6/CD1 genetic background. Details on the generation of recombinant and experimental MADM mice are described Figure S3.

Heterozygote $Lis1^{+/-}$ (Hirotsune et al., 1998), $Ndel1^{+/-}$ (Sasaki et al., 2005), and $14\text{-}3\text{-}3\varepsilon^{+/-}$ (Toyo-oka et al., 2003); $Emx1^{Cre/+}$ (Gorski et al., 2002); $Nestin\text{-}CreER^{+/-}$ (Imayoshi et al., 2006) and $Rosa26^{Flpe/+}$ (Farley et al., 2000) mice have been described previously. Timed pregnancies were setup to generate embryos and mice at defined developmental stages as indicated throughout the study.

All experimental procedures involving the above listed mice were carried out in accordance with the APLAC (Administrative Panel on Laboratory Animal Care) protocol and the institutional guidelines by the Veterinary Service Center (VSC) at Stanford University.

Generation of Recombinant Mice for MADM Analysis

Mouse breeding for generation of recombinant mice was carried out according to the scheme in Figure S3. The scale of the mating for generating recombinants using meiotic recombination was adjusted according to the genetic distance between the MADM cassettes and the gene of interest. In particular, MADM-11 cassettes are ~3 cM (centi-Morgan) distal to the centromere while for example *Lis1* is located ~44 cM distal to the centromere, or ~41 cM away from the MADM cassettes. Thus, there is 41% probability that meiotic recombination will occur in the recombinant generating mating (Figure S3). However, since only half of the progeny will be of the desired genotype (TG,mutant), while the other half will be wild-type (+,+), animals with the appropriate genotype will be generated at a rate of ~20% (41% x ½). Upon recombination of the mutant onto the TG-containing MADM chromosome, mutant cells are labeled in green and wild-type control cells in red (see also Figure S3C for *Ndel1* mutant). A similar crossing strategy using the reciprocal MADM cassette (GT) in the crosses described above is typically used to generate mice ready for MADM analysis with labeling of mutant and wild-type cells in the 'opposite' direction (mutant in red and wild-type control in green, see also Figure S3C and S3D). Generally, performance of MADM analysis in both directions with reciprocal labeling scenarios should eliminate any possible bias.

Live-Imaging Assay for MADM-Labeled Organotypic Slices

Whole E14.5 MADM-labeled brains (control- and *Ndel1*-MADM) were isolated and 350μm coronal slices obtained using a vibratome (Leica). Slices were transferred to transparent cell culture filter insets (Millipore) and cultured in DMEM/F12 medium containing 1X N2 supplement (Gibco) for 1-2h in glass-bottom 6-well plates (MatTek) prior to live-imaging sessions lasting typically 10-15h (individual frames at 10-15min.) using an inverted confocal microscope equipped with an environmental chamber (Leica). Movies for analysis of cell migration were generated using Leica TCS SP5 software. Average speed of migration (μm/h) was determined by measurement of the distance travelled during the time period of active locomotion of migrating cortical projection neurons (derived from 3 independent movies). IZ-CP borders were determined by bright field microscopy based on the cell density difference. Quantifications of neurite length and branch numbers were carried out as previously described (Youn et al., 2009). Values represent mean ± SEM. Student's *t*-test was used to determine significance with ***p<0.001.

Total Cell Numbers for Quantification of Phenotypes and Statistical Analyses

Total cell numbers that were included in the quantification charts throughout the study were:

Figure 2 (control-MADM: 4667; *Lis1*-MADM: 2750; *Ndel1*-MADM: 4923; *14-3-3ε*-MADM: 3242). Figure 3 (control-MADM: 529; *Lis1*-MADM: 307; *Ndel1*-MADM: 602; *14-3-3ε*-MADM: 481). Figure 4 (control-MADM: 475 in RMS, 876 in OB; *Ndel1*-MADM: 1076 in RMS, 705 in OB). Figure 5 (control-MADM: 94 Purkinje cells, 574 cGCs; *Ndel1*-MADM: 306 Purkinje cells, 1651 cGCs). Figure 6 (control-MADM: 3604; *Ndel1*-MADM: 3891; clonal-MADM: 756). Figure 7 (*Ndel1*-MADM: 341). Figure S4 (*Lis1*-MADM: 4112). Figure S5 (control-MADM: 387; *Lis1*-MADM: 236; *Ndel1*-MADM: 716; *14-3-3ε*-MADM: 289). Figure S6 (*14-3-3ε*-MADM: 298 in OB; 107 Purkinje cells, 1216 cGCs). Figure S8 (control-MADM: 30; *Lis1*-MADM: 43; *Ndel1*-MADM: 63; *14-3-3ε*-MADM: 36). Values in all graphs and charts generally represent mean ± SEM. Student's *t*-test was used to determine significance with *p<0.05, **p<0.01, and ***p<0.001.

Possible Effect of Perdurance in Mosaic Analysis

In MADM analysis, it is possible that the perdurance of remnant mRNA and/or protein from parental heterozygous cells may provide residual *Ndel1* function, which could in principle support a certain level of neuronal migration in the *Ndel1*$^{-/-}$ cells. However, the following lines of evidence strongly argue against the possibility that perdurance of *Ndel1* contributes significantly to the phenotypic difference between our sparse knockout and genetic perturbations of *Ndel1*. The *Emx1-Cre* and *Nestin-spCre* drivers that we used to generate MADM clones induce recombination well before the *hGFAP-Cre* (Zhuo et al., 2001) (which is not active before E12.5/E13.5 in cortical RGPC) used for whole cortex *Ndel1* knockout using the same mutant allele (Youn et al., 2009). Yet live imaging of *hGFAP-Cre* induced *Ndel1* knockout neurons fail to migrate in E14.5 slices (Youn et al., 2009), whereas live imaging of MADM knockout *Ndel1* neurons under similar imaging conditions show an average migration speed indistinguishable

from control neurons (Figure 7Q). Furthermore, we have generated TM-induced MADM-clones as early as E8 (Figure 6M). These early E8 clones included dozens of MADM-labeled *Ndel1*$^{-/-}$ neurons - residual *Ndel1* mRNA and/or NDEL1 protein would have been serially diluted to a few percent even without degradation. For example, in all MADM experiments, the mitotically active 'mother' progenitor cell is heterozygous (starting with ~50%) and after 4 divisions, one could expect maximal RNA/protein perdurance to be less than 5%. Nevertheless, *Ndel1*$^{-/-}$ neurons from early E8 induced clones exited the VZ/SVZ properly and migrated across the IZ without significant defects when compared to labeled control neurons. However, TM-induced conditional whole cortex knockout of *Ndel1* one day prior to live-imaging at E14.5 results in a complete block of neuronal migration (Youn et al., 2009), indicating minimal perdurance of *Ndel1* activity even within a day after gene inactivation.

For *Lis1* mosaic analysis, it is possible that the 10% or so remaining *Lis1*$^{-/-}$ neurons observed in *Lis1*-MADM were direct progeny of *Lis1*$^{+/-}$ progenitors undergoing the final cell division and therefore could have the highest perdurance. Significant perdurance in a fraction of *Lis1*$^{-/-}$ neurons may allow those neurons to migrate into and within the cortical plate. However, several lines of evidence argue against this interpretation. First, neuronal migration is extremely sensitive to *Lis1* dosage and neurons with ~35% of LIS1 protein show significant deficits in migration (Gambello et al., 2003; Hirotsune et al., 1998). Second, conditional deletion of *Lis1* in the cortex resulted in complete block of migration within a day (Youn et al., 2009). Third, *Lis1*$^{-/-}$ cortical projection neurons exhibited a significant migration delay when examined at P1, and somehow "caught up" with *Lis1*$^{+/-}$ neurons at P7 and P21 (Figure S3). Perdurance would result in an opposite time-dependence.

For all of the above reasons, we consider that potential perdurance of NDEL1 or LIS1 cannot account for the difference of phenotypes we observed in sparse knockout and previous cortical knockout. Rather, these differences are most likely caused by cell-non-autonomous effect.

SUPPLEMENTAL REFERENCES

Farley, F.W., Soriano, P., Steffen, L.S., and Dymecki, S.M. (2000). Widespread recombinase expression using FLPeR (flipper) mice. Genesis *28*, 106-110.

Gambello, M.J., Darling, D.L., Yingling, J., Tanaka, T., Gleeson, J.G., and Wynshaw-Boris, A. (2003). Multiple dose-dependent effects of Lis1 on cerebral cortical development. J Neurosci *23*, 1719-1729.

Gorski, J.A., Talley, T., Qiu, M., Puelles, L., Rubenstein, J.L., and Jones, K.R. (2002). Cortical excitatory neurons and glia, but not GABAergic neurons, are produced in the Emx1-expressing lineage. J Neurosci *22*, 6309-6314.

Hirotsune, S., Fleck, M.W., Gambello, M.J., Bix, G.J., Chen, A., Clark, G.D., Ledbetter, D.H., McBain, C.J., and Wynshaw-Boris, A. (1998). Graded reduction of Pafah1b1 (Lis1) activity results in neuronal migration defects and early embryonic lethality. Nat Genet *19*, 333-339.

Imayoshi, I., Ohtsuka, T., Metzger, D., Chambon, P., and Kageyama, R. (2006). Temporal regulation of Cre recombinase activity in neural stem cells. Genesis *44*, 233-238.

Sasaki, S., Mori, D., Toyo-oka, K., Chen, A., Garrett-Beal, L., Muramatsu, M., Miyagawa, S., Hiraiwa, N., Yoshiki, A., Wynshaw-Boris, A*., et al.* (2005). Complete loss of Ndel1 results in neuronal migration defects and early embryonic lethality. Mol Cell Biol *25*, 7812-7827.

Shaner, N.C., Campbell, R.E., Steinbach, P.A., Giepmans, B.N., Palmer, A.E., and Tsien, R.Y. (2004). Improved monomeric red, orange and yellow fluorescent proteins derived from Discosoma sp. red fluorescent protein. Nat Biotechnol *22*, 1567-1572.

Toyo-oka, K., Shionoya, A., Gambello, M.J., Cardoso, C., Leventer, R., Ward, H.L., Ayala, R., Tsai, L.H., Dobyns, W., Ledbetter, D*., et al.* (2003). 14-3-3epsilon is important for neuronal migration by binding to NUDEL: a molecular explanation for Miller-Dieker syndrome. Nat Genet *34*, 274-285.

Youn, Y.H., Pramparo, T., Hirotsune, S., and Wynshaw-Boris, A. (2009). Distinct dose-dependent cortical neuronal migration and neurite extension defects in Lis1 and Ndel1 mutant mice. J Neurosci *29*, 15520-15530.

Zheng, B., Sage, M., Cai, W.W., Thompson, D.M., Tavsanli, B.C., Cheah, Y.C., and Bradley, A. (1999). Engineering a mouse balancer chromosome. Nat Genet *22*, 375-378.

Zheng, B., Sage, M., Sheppeard, E.A., Jurecic, V., and Bradley, A. (2000). Engineering mouse chromosomes with Cre-loxP: range, efficiency, and somatic applications. Mol Cell Biol *20*, 648-655.

Zhuo, L., Theis, M., Alvarez-Maya, I., Brenner, M., Willecke, K., and Messing, A. (2001). hGFAP-cre transgenic mice for manipulation of glial and neuronal function in vivo. Genesis *31*, 85-94.

Zong, H., Espinosa, J.S., Su, H.H., Muzumdar, M.D., and Luo, L. (2005). Mosaic analysis with double markers in mice. Cell *121*, 479-492.